Achieving Reliable and Repeatable Electrochemical Impedance Spectroscopy of Rechargeable Batteries at Extra-Low Frequencies

Christopher Dunn and Jonathan Scott, *Life Senior Member, IEEE*

***Abstract*—There is a need for techniques for efficient and accurate measurement of the impedance of rechargeable batteries at extra-low frequencies (ELFs, of the order of microhertz), as these reflect real usage and cycling patterns, and their importance in fractional battery circuit modeling is becoming increasingly apparent. Major impediments include the time required to perform such measurements, and 'drift' in impedance values when measurements are taken from the same battery at different times. Moreover, commercial impedance analyzers are generally unable to measure at these frequencies. We describe here our use of programmable two-quadrant power supplies to deliver multiple small signal measurement tones in the presence of large signal 'working' currents, and our use of these data to generate impedance measurements with good precision and in reasonable time. The improvement in quality of electrochemical impedance spectroscopy data is verified through root mean square error when fitting equivalent-circuit models.**

***Index Terms*—Rechargeable batteries, electrochemical impedance spectroscopy, impedance, measurement, extra-low frequency, equivalent-circuit model.**

I. Introduction

ELECTROCHEMICAL impedance spectroscopy (EIS) is a powerful and non-destructive tool by which the properties and characteristics of a battery can be deduced by determining impedance over a wide frequency range [1], [2]. EIS is claimed to be a reliable indicator of state of charge (SoC) [3], [4], and state of health (SoH) [5]. The battery research community has traditionally tended to focus heavily on equivalent-circuit models (ECMs) fitted to EIS data. These circuit models are considered key to prediction of SoC and SoH [2], [5]–[8], although the reliability of some claims, particularly around SoC, are questioned by some authors (see Mauracher and Karden [9], for example).

Impedance spectra can be presented either as Bode plots or Argand diagrams (also called Nyquist plots). Bode plots are now considered to be more informative [1]. This is because frequency information is implied rather than shown explicitly in Nyquist plots, while Bode plots contain all necessary detail [2], [7], [10]. This manuscript will use Bode plots exclusively.

Mauracher and Karden noted as long ago as 1997 that rechargeable batteries ought to be measured and characterized at frequencies that reflect their usage patterns [9]. These authors suggested that measuring down to $10\,\mu\mathrm{Hz}$, representing a period of approximately 28 hours, yielded useful information relating to diffusion outside the electrodes in a battery. Measurements taken at these extra-low frequencies (ELFs) provide insights into model formulation [11] and have been shown to aid model fitting [12]. The use of ELFs is new, which is surprising because rechargeable batteries are often found in appliances that are charged daily, which corresponds to a cycling frequency of approximately $11.6\,\mu\mathrm{Hz}$.

Measuring in the ELF range is associated with a number of difficulties. These include the time needed to make the measurement. The minimum practical period for an EIS measurement is the reciprocal of its frequency. To minimize the time required, a single stimulus signal that includes all frequencies of interest can be used [13]. The magnitudes and phases of voltages and currents at these frequencies can be recovered by using a Fourier transform. In this case the stimulus is referred to as a multitone or multisine. Other complex waveforms can be used to find impedances at multiple frequencies, for example a pseudo-random binary sequence (PRBS) [14], [15], although there is a tradeoff between increasing numbers of frequencies and the signal-to-noise ratio (SNR) of the measurement.

Researchers have been faced with difficulties in finding equipment suitable for operation at ELFs. Almost all commercial impedance meters have a lower frequency limit of $1\,\mathrm{mHz}$, which may have something to do with the many investigators reporting results obtained at frequencies no lower than this [16]–[23]. The Solartron 1260A is rated to measure down to $10\,\mu\mathrm{Hz}$, but its use has been found to require great care when working with 'wet' systems such as batteries [13].

Modern electrochemical theory accepts that batteries exhibit 'fractional capacitance' [24], and an ECM should therefore contain constant phase elements (CPEs) in order to embody battery characteristics [12], [13], [25]. Fractional components are associated with long decay tails after a stimulus is applied or removed [26], [27], and these tails are thought to be among the problems encountered when measuring 'wet' systems with the Solartron [13].

The impedance of a battery is known to 'drift'. Figure 1 shows EIS data obtained at five frequencies from a near-new $30\,\mathrm{Ah}$ absorbent glass mat (AGM) lead-acid battery of the type typically found in light traction and power backup

The authors are with the School of Engineering, University of Waikato, Private Bag 3105, Hamilton 3240, New Zealand. E-mail: cjdunn@xtra.co.nz

Manuscript received February 9, 2022; revised April 6, 2022.

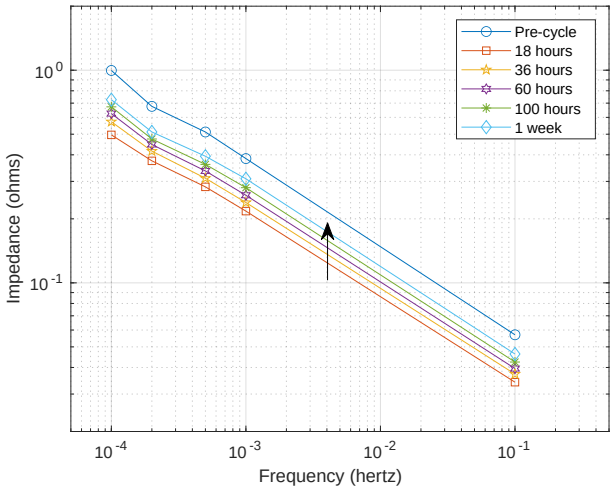

Fig. 1. Impedance (magnitude) of a 30 Ah AGM lead-acid battery at five frequencies before and at various times after a charge-discharge cycle at 5 A. The arrow shows the impedance drift over time as the battery equilibrates.

applications. Measurements were made before and at several times after cycling the battery and returning it to 80% SoC. Note that the small-signal impedance of the battery is halved by cycling, with over a week being required for the battery to re-equilibrate and return to its original state. Other reported transient phenomena include the 'coup de fouet' ('crack of the whip'), which causes a sudden drop in voltage and change in impedance with subsequent recovery when a fully charged lead-acid battery is initially discharged [28].

We have observed impedance drifts in other battery chemistries, including the lithium family, although relaxation times seem to be much shorter. These drifts, which have been noted by other researchers [29], make observation more difficult and add to the frustration experienced by researchers seeking reliable, repeatable EIS data. This manuscript presents novel measurement strategies that address these problems, and demonstrates the importance of measured data quality in battery characterization and accurate ECM fitting.

II. New Methods For Battery Impedance Measurement

All data obtained from the new system were measured at 22 °C with two-quadrant precision sources using four-wire connections controlled via GPIB interfaces by Raspberry Pi 4 computers running custom software written in C. The software utilities are (i) bz3p66 and (ii) bzdcp66 (battery impedance with (i) triphasic pulses or (ii) added dc component on our 'Prologix/66332A' hardware) [30]. These command line programs, which are called by scripts setting the parameters for each run, minimize the risk of interference between a small measurement signal and large 'working' current signal by using time division or frequency division multiplexing, respectively. Both programs make multitone impedance measurements by sourcing and sinking current and recording times, currents and voltages in three-column '.tvi' data files

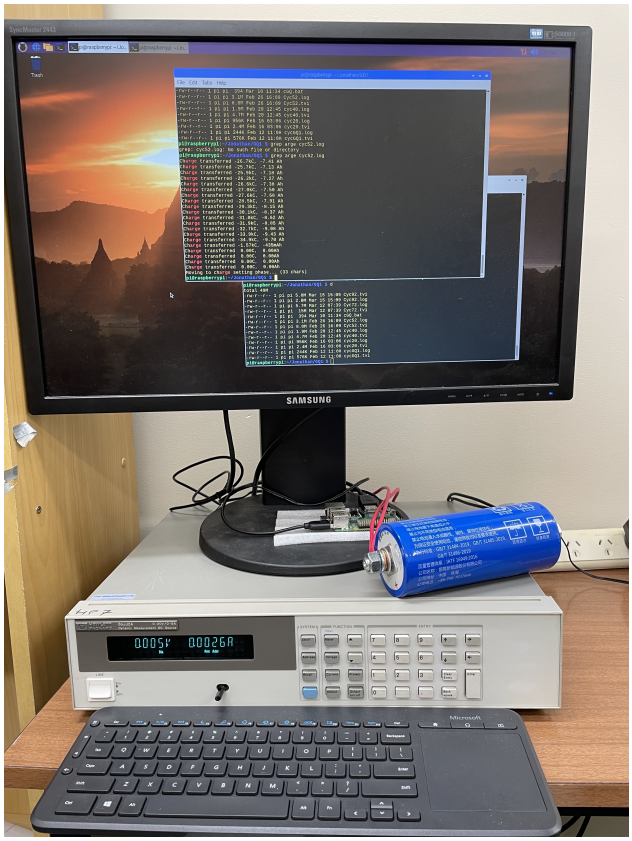

Fig. 2. An example measurement system set up to use an HP66332A. Note the unenclosed Raspberry Pi model 4 on the monitor base. The blue cylinder is the battery under test, a single 40 Ah LTO cell.

(timestamp, voltage, current). Default frequency ranges are 1-2-5 sequences between minimum and maximum specified values, but any set of frequencies is possible. The complex impedance $Z(\omega)$ for each frequency of interest,

$$\text{where } Z(\omega) = \frac{|V|}{|I|} e^{j(\phi_V - \phi_I)},$$

is obtained from the .tvi data by performing a discrete Fourier transform with 'dftv', a program based on software originally described by Scott and Parker [31] for use with SPICE.

The battery used in the new ELF experiments was a brand new lithium titanate (LTO) 40 Ah 2.3 V 66160H cell. Figure 2 depicts the equipment setup. Figure 3 presents a block diagram of the system. Measurement parameters were based on our experience of battery cycling and impedance measurement, the manufacturer's ratings for the battery under test, and the capabilities of the 66332A units.

A. Time Division Multiplexing: bz3p66

bz3p66 alternately subjects the battery to a small-signal measurement multitone and a 'working' stimulus signal that reflects a normal usage current. Interference is minimized by reducing as far as possible the change in terminal voltage that is seen following the application of a large working signal (i.e. minimizing the artefact or 'pulse tail' that characterizes fractional elements as described earlier [27]). The working stimulus is a triphasic pulse, a stimulus believed

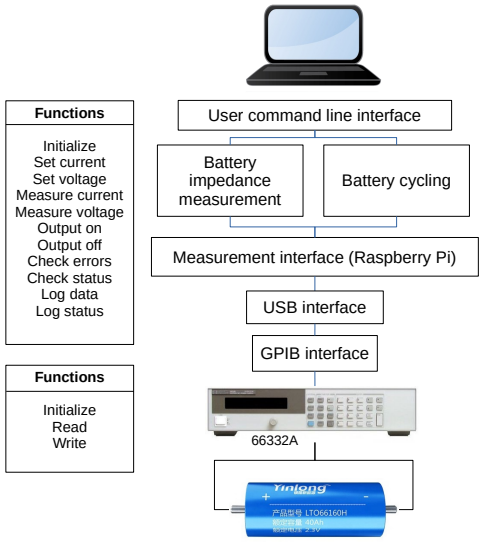

Fig. 3. Measurement system architecture.

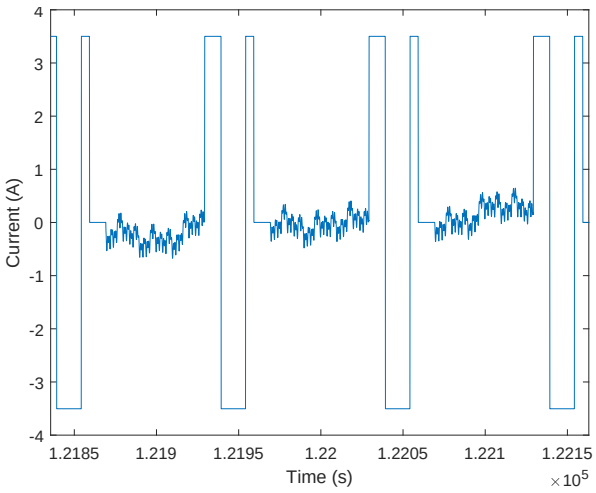

Fig. 4. Time domain plot: bz3p66 on LTO, 30-second ± 3.5 A triphasic pulse every minute. Note the 10-second 'rest' after the end of each pulse to allow for settling of the long voltage tail that characterizes fractional devices, and the small signal measurement tones between the pulses.

from empirical observations in human-implanted electrodes to minimize artefact tails [26]. Some mathematics confirm that the optimal pulse in a fractional derivative system consists of three equal amplitude, alternating-polarity pulses in a 2-3-1 duration sequence (Figure 4).

bz3p66 outputs two time domain files, one that includes the triphasic pulse ('.ptvi') and one with the pulse removed: this is the .tvi file that is used for further analysis.

The LTO battery was cycled once using a constant current-constant voltage (CCCV) regime. Maximum (V_{max}) and minimum (V_{min}) CV voltages were set at 2.7 V and 1.8 V, respectively; the charge and discharge CC currents were 5 A (the maximum available from the 66332A units). CV phases were ended at ± 1 A. The battery was rested after cycling for 10 minutes at a final SoC of 65%. Following this, bz3p66 was

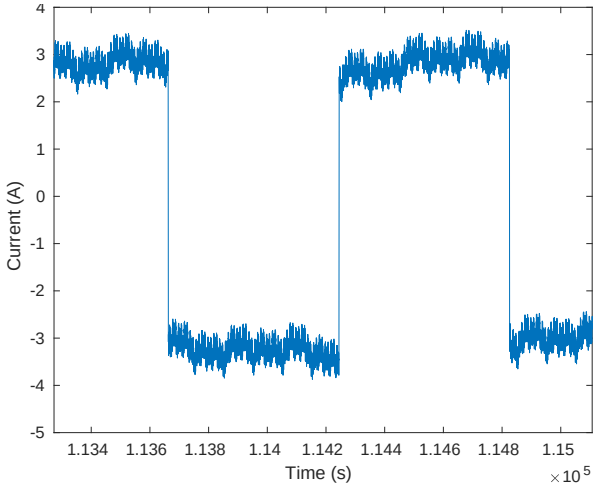

Fig. 5. Time domain plot: bzdcp66 on LTO, ± 3 A 860 µHz square wave. Note offset measurement tones.

run four times with working ± 3.5 A current pulses as follows:

1) 30-second pulse every 4 minutes;
2) 30-second pulse every 2 minutes;
3) 30-second pulse every minute (see Figure 4);
4) 60-second pulse every 2 minutes.

Measurement tones were 1-2-5 sequences from 10 µHz (three cycles) to 1 Hz. The maximum total charge that could be sourced or sunk (dQ_{max}) was set at 5 Ah (0.125C). This charge is distributed across all measurement tones.

B. Frequency Division Multiplexing: bzdcp66

bzdcp66 performs battery measurements by exposing the battery to a small signal multitone and a working stimulus signal simultaneously. This is accomplished by superimposing the EIS multitone on a periodic square wave which aims to mimic the effect of a working dc signal (Figure 5).

The battery was cycled to 65% SoC as for bz3p66 and then subjected to sets of consecutive bzdcp66 runs as follows:

1) three runs with 3 A square wave (I_{dc}) at a frequency of 860 µHz (f_{dc}), i.e. a period of approximately 20 minutes;
2) three runs with I_{dc} 35 mA with the same f_{dc} (i.e. negligible working current signal);
3) cycle again to reset and ensure SoC;
4) repeat.

Measurement tones were 1-2-5 sequences from 20 µHz (three cycles) to 2 Hz. dQ_{max} was 5 Ah, distributed across all measurement tones as with bz3p66.

The working and EIS signals for bzdcp66 are selected so that their spectra do not overlap. This is done by choosing EIS frequencies that are multiples of f_0, the lowest frequency, and powers of 2 or 5:

$$f_{test} = 2^p \times 5^q \times f_0 \tag{1}$$

where f_{test} is a test frequency, and p and q are integers. Thus, each frequency in the multisine has the prime factors 2 and 5 only in its multiple of f_0. The square wave is then given a

frequency that is a multiple of f_0 but that does not have 2 or 5 as prime factors, for example:

$$f_{dc} = 7^i \times 11^j \times 13^k \times 17^l \times f_0 \quad (2)$$

where i, j, k and l are integers. This suggests that f_{dc} might be a multiple of 7, 11, 13, 17, etc.

As a final check, all odd multiples of f_{dc} can be compared with each multisine tone, and a larger factor chosen for f_{dc} if there are 'near miss' differences that might pollute adjacent tones in a windowed Fourier transform. For these experiments, $860\,\mu\text{Hz}$ was chosen as this is a multiple of 43 (a prime number) and the fundamental frequency of $10\,\mu\text{Hz}$, and has no harmonics close to any of the test frequencies.

C. Data Quality Evaluation: ECM Fitting

The quality of the data was evaluated via ECM fitting. The procedure used was developed at this center and has been described recently by Poihipi et al. [12]. Briefly, the measured data are used to generate an ECM via an optimization method based on the downhill simplex algorithm of Nelder and Mead and implemented in C as a command line program [32], [33].

The optimization target is defined as a root mean square error (RMSE) value calculated from complex impedances as indicated by the measured data. The final RMSE reflects how well the the model fits the data: a perfect fit will yield an RMSE approaching zero; higher values indicate noisier (less stable) data. The choice of appropriate model starts with the simplest ECM which is based on a single resistor and CPE in series (R-CPE). If the resulting RMSE indicates a poor fit, selection moves to the next model in the chain of complexity, a resistor and two CPEs in series (R-CPE-CPE). Fitting then starts with parameter values returned by the R-CPE case. If the previous fit had resulted in an RMSE dictated chiefly by noise in the data, the additional component will not improve the fit and the quality of the data can be said not to justify the more complicated model, even if that model is in fact more correct. If the additional element reduces the RMSE, however, we may conclude that the extended model represents the data better. The reader is referred to Poihipi et al. [12] for more details of the ECM fitting method.

III. Results

A. Time Division Multiplexing: bz3p66

Impedance magnitude and phase curves obtained from the Fourier-transformed .tvi data generated by bz3p66 are shown in Figure 6. Varying the duration and/or frequency of the triphasic pulse made little or no difference to magnitude and phase profiles, with consistent disturbance of the phase response around $0.1\,\text{mHz}$.

Different regions of the Bode plot reveal various aspects of the battery's characteristics and condition that can be represented in an ECM. Briefly, the high frequency section of the magnitude plot approaches a horizontal asymptote that represents the series resistance (R_s) of the battery, while the region below $1\,\text{mHz}$ is dominated by a CPE (i.e. the R-CPE model). Other behaviors of the magnitude and phase plots reveal hints as to other circuit elements that might be

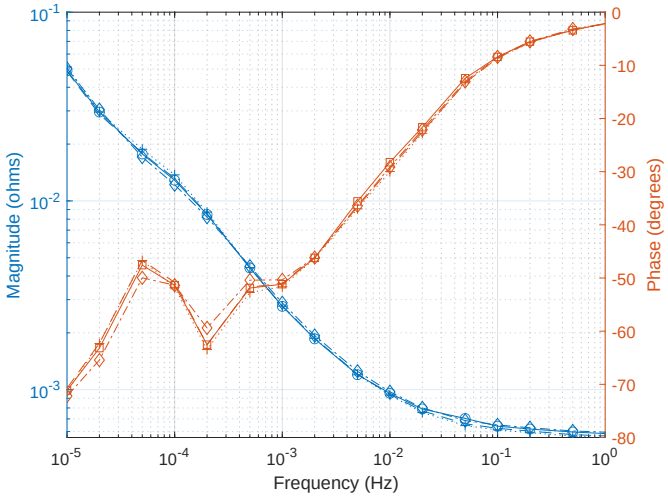

Fig. 6. bz3p66 on LTO battery: impedance magnitude and phase of four runs with differing triphasic pulse frequencies and durations. Solid lines, open circles (magnitude) or squares (phase) = 30-second pulse repeated every minute; dashed lines = 30-second pulse every 2 minutes; dotted lines with crosses = 30-second pulse every 4 minutes; dot-dash lines with open diamonds = 60-second pulse every 2 minutes. On this and all subsequent plots magnitude runs from top left to bottom right, and phase from bottom left to top right.

appropriate. For example, the rounded 'knee' between the R_s and first CPE regions suggests a second fractional series element [12], [13], [27] (i.e. the R-CPE-CPE model). Results showing the relationship between the quality of the measured data and ECM determination are summarized later (see III-D).

B. Frequency Division Multiplexing: bzdcp66

Figures 7 and 8 show impedance magnitude and phase curves overlaid from repeated runs (three plots per chart to maintain clarity) of bzdcp66 with a $3\,\text{A}$ working square wave. Magnitude and phase appeared consistent and repeatable between runs, whether interspersed with additional cycling or not, and the low frequency phase response did not show the disturbance exhibited repeatedly by bz3p66.

Similar consistency between runs was noted when bzdcp66 was run with a negligible ($35\,\text{mA}$) square wave to mimic a small signal measurement multitone with no working current (Figures 9 and 10). No impedance drift due to re-equilibration after cycling as described earlier in lead-acid batteries (Figure 1) was evident. These results are consistent with observations that suggest very rapid re-equilibration of batteries based on lithium chemistries. Interestingly, the phase irregularity around $0.1\,\text{mHz}$ seen with time division multiplexing reappeared in the presence of negligible I_{dc}.

C. Comparison of Time Division and Frequency Division Multiplexing: bz3p66 vs bzdcp66

In view of the homogeneity between sweeps for each type of measurement (i.e. bz3p66 and bzdcp66 with or without a working square wave), individual representative plots may be used for visual comparison of the different methods. Figure 11

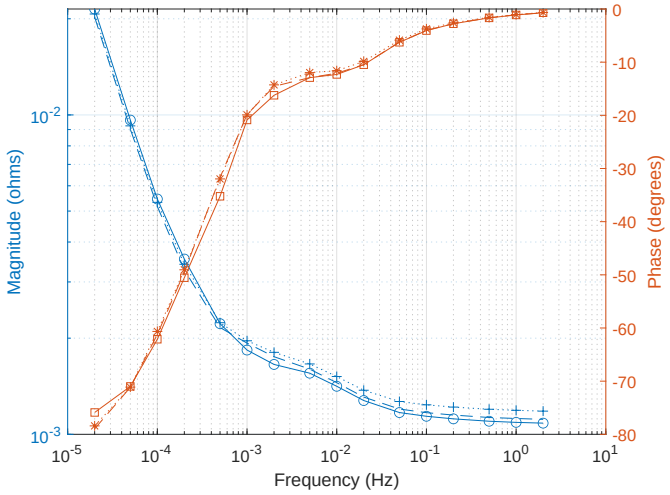

Fig. 7. Impedance magnitude and phase: bzdcp66 on LTO battery with 3 A square wave. The battery was cycled twice, with three consecutive impedance measurements after each cycling. Solid lines with open circle (magnitude) or square (phase) = first of three consecutive impedance measurements after first cycling; dashed lines = third of three consecutive measurements after first cycling; dotted lines with star/asterisk = second of three consecutive measurements after second cycling.

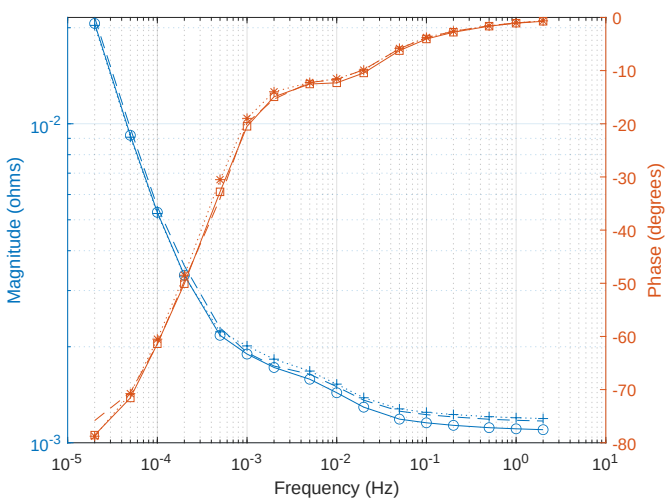

Fig. 8. Impedance magnitude and phase: bzdcp66 on LTO battery with 3 A square wave. Solid lines with open circle (magnitude) or square (phase) = second of three consecutive impedance measurements after first cycling; dashed lines = first of three consecutive measurements after second cycling; dotted lines with star/asterisk = third of three consecutive measurements after second cycling.

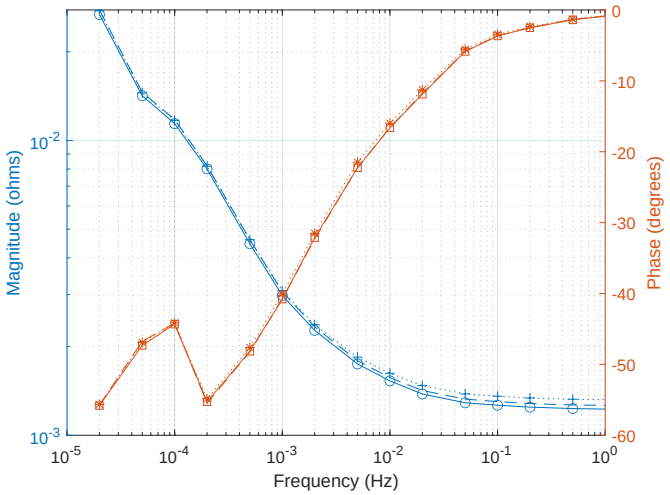

Fig. 9. Impedance magnitude and phase: bzdcp66 on LTO battery with 35 mA square wave. Solid lines with open circle (magnitude) or square (phase) = first of three consecutive impedance measurements after first cycling; dashed lines = third of three consecutive measurements after first cycling; dotted lines with star/asterisk = second of three consecutive measurements after second cycling.

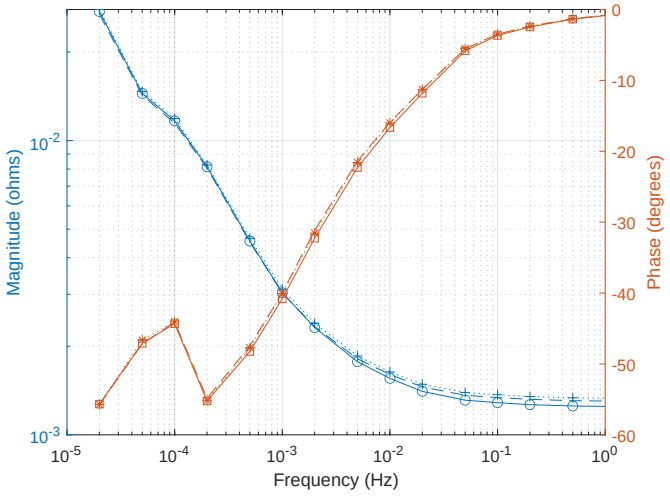

Fig. 10. Impedance magnitude and phase: bzdcp66 on LTO battery with 35 mA square wave. Solid lines with open circle (magnitude) or square (phase) = second of three consecutive impedance measurements after first cycling; dashed lines = first of three consecutive measurements after second cycling; dotted lines with star/asterisk = third of three consecutive measurements after second cycling.

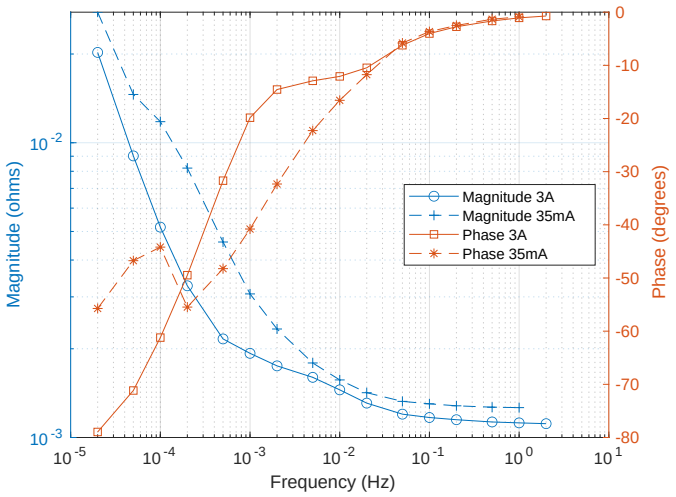

Fig. 11. Impedance magnitude and phase plots: representative bzdcp66 runs (third of three sweeps for each square wave magnitude) on LTO battery with 3 A and 35 mA square waves. The solid lines with open symbols show magnitude and phase achieved with a 3 A square wave; the dashed lines with star/asterisk show results with a 35 mA (i.e. negligible) square wave.

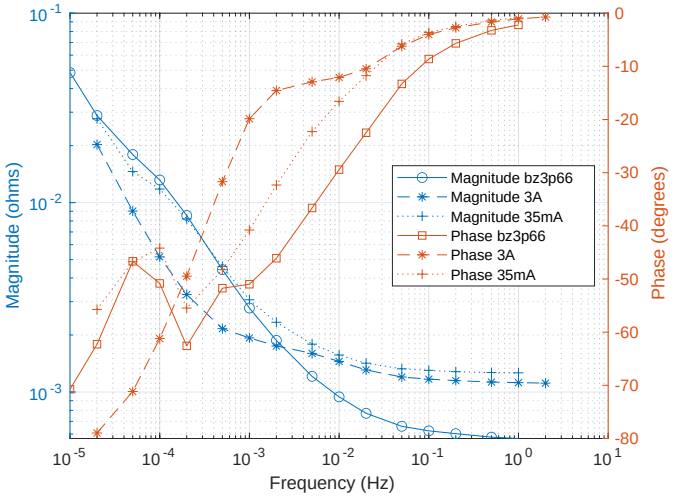

Fig. 12. Impedance magnitude and phase plots: comparison of bzdcp66 with a 3 A or 35 mA square wave and bz3p66 runs on LTO battery. Solid lines with open symbols = bz3p66 sweep with a 30-second triphasic pulse every 2 minutes; dashed lines with asterisks = third of three bzdcp66 sweeps with a 3 A square wave; dotted lines with crosses = third of three bzdcp66 sweeps with a 35 mA square wave.

contrasts third (final) runs from one set each of bzdcp66 runs with 3 A and 35 mA working currents.

Note the reduction in impedance magnitude when a significant working signal is applied, particularly in the region below 0.5 mHz (e.g. 0.0052 ohm vs 0.0118 ohm at 0.1 mHz), and the elimination of erratic behavior in the low frequency region of the phase plot. Additional shaping of the phase curve is also evident in the region around 10 mHz in the presence of a 3 A working current. This is not visible when the square wave is effectively 'turned off', and implies the availability of additional information that might be important in the development of a realistic ECM for the battery.

Finally, Figure 12 repeats the above with the addition of magnitude and phase information from a representative bz3p66 run (30-second pulse every 2 minutes). The magnitude trace follows that of bzdcp66 with negligible square wave in the low frequency region, but with markedly erratic phase behavior. Most notable, however, is the suppression of impedance magnitude in the higher frequency R_s region.

D. ECM Fitting

Table I summarizes the results of ECM fitting to data obtained using the three measurement techniques described above. Data from all runs with each type of measurement (bzdcp66 with 3 A square wave, bzdcp66 with 35 mA square wave, and all triphasic pulse variations of bz3p66) were respectively concatenated into three combined files for the analysis, one for each type of measurement.

Observing the changes in parameter values and RMSEs when attempting to develop the model from the basic R-CPE case (Table I), only bzdcp66 with a 3 A working square wave yielded data that allowed the second CPE to be 'seen'. This level of model refinement was not possible with either bzdcp66 with a 35 mA square wave or bz3p66, as shown by the negligible changes in parameter values upon addition of the second CPE. Note also the identical RMSEs for the R-CPE and R-CPE-CPE models with these two last measurement techniques, with α values approaching zero for the second CPE (Table I). In contrast, addition of the second CPE when fitting to data generated by bzdcp66 with 3 A working current resulted in a halving of the RMSE value (Table I).

TABLE I
ECM PARAMETER ESTIMATION

ECM	R_s	α	C_F	C_2	α_2	RMSE
bzdcp66 3 A square wave (frequency multiplexing)						
R-CPE	1.252	0.80	73,270			0.1271
R-CPE-CPE	0.406	0.91	17,130	1218	0.07911	0.0651
bzdcp66 35 mA square wave (frequency multiplexing)						
R-CPE	1.228	0.63	10,280			0.0804
R-CPE-CPE	1.069	0.63	10,300	6236	0.00004	0.0804
bz3p66 (time multiplexing)						
R-CPE	0.559	0.66	11,330			0.1020
R-CPE-CPE	0.434	0.66	11,290	8042	0.00006	0.1020

CPE, constant phase element; ECM, equivalent-circuit model; RMSE, root mean square error.
R_s, series resistance ($ohm \times 10^{-3}$); C_F and C_2, fractional capacitances ($F/s^{(1-\alpha)}$) of first (R-CPE model) and second (R-CPE-CPE model) CPEs, with respective slopes denoted by α and α_2.

IV. Discussion

Evidently, charge density or rates of current flow must be taken into account when measuring impedance and parameterizing models. Apparent impedance decreases when higher currents are passed, an effect that is exaggerated at low frequencies. Figure 13 shows data from an exploratory experiment in which $|Z|$ was measured using a multisine run at maximum current (I_{max}) values ranging from 5 mA to 7 A

on a lithium iron phosphate battery rated at 4 Ah. Frequencies ranged from 200 µHz to 100 mHz. Measurements from 50 mA to 200 mA (approximately C/50) behaved like 'small' signals. At higher frequencies, increasing current had less effect, but although the 7 A maximum current had a marked effect on the low frequency traces, it did not 'pull' the impedance down to a high current asymptote, which suggests some permanent resistive mechanism that cannot be overcome. This is more apparent in Figure 14, which shows full frequency sweeps carried out with I_{max} set at 50 mA and 7 A after cycling.

Unfortunately, it is not possible to draw substantial current from a battery for prolonged periods because the battery will run flat, a major difficulty encountered by Budde-Meiwes et al. [29]. As described by Scott and Hasan [13], the peak amplitude of charge delivered is dependent on the frequency of the signal. As frequency decreases, the current stimulus must be dropped significantly to prevent the charge excursion flattening or overcharging the battery. Budde-Meiwes et al. [29] abandoned ELF measurements because it is not possible to make a reliable measurement of battery impedance below 1 mHz without running for periods well in excess of 1000 seconds. Overall, the twin aims of measuring at ELFs while the battery under test is delivering significant current cannot be met with techniques that have been available until now. In this manuscript we have described two methods permitting ELF measurements while the battery is delivering or receiving substantial current or charge without going flat or overcharging.

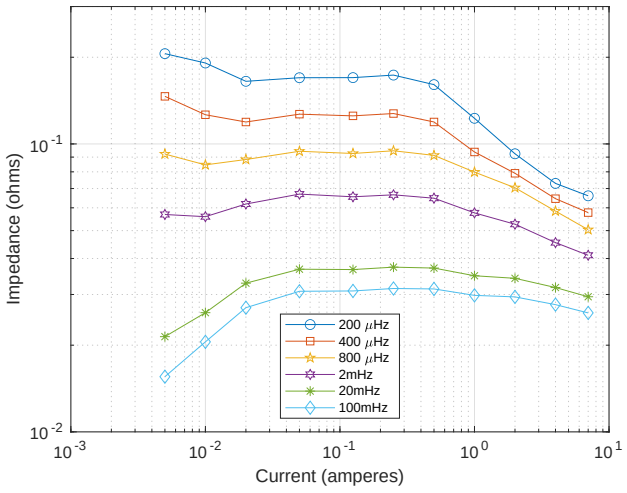

Fig. 13. Impedance of a 4 Ah $LiFePO_4$ battery plotted against currents ranging from 5 mA to 7 A at six frequencies (see figure legend). Measurements taken on a Keithley 2460A four-quadrant precision source controlled by a Raspberry Pi running custom software [30].

V. Conclusion

We have presented two novel methods for measuring the impedance of batteries at ELFs in the presence of substantial currents. One method time-division multiplexes EIS measurement stimuli with large 'working' current bursts, the second method multiplexes in the frequency domain, relying on Fourier transformation to recover the EIS data from 'underneath' the large working current. Both methods break the fundamental limiting tradeoff noted by Budde-Meiwes et al. [29] between the magnitude of the 'working' current that can be drawn during measurement and the lowest attainable frequency in the EIS. We show here measurements to 10 µHz, and note that exploratory measurements to below 500 nanohertz have been made.

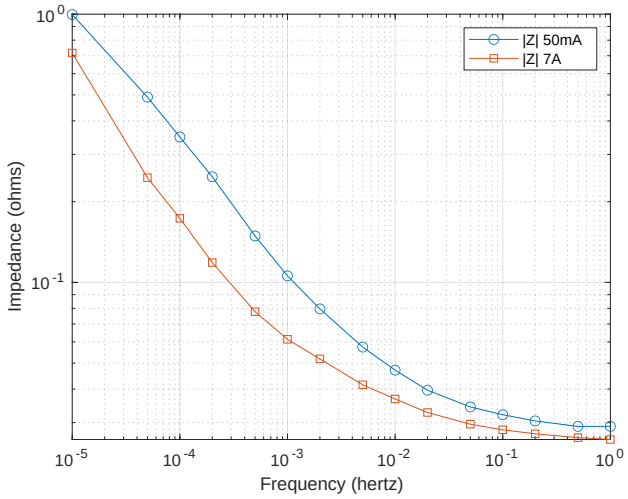

Fig. 14. Impedance versus frequency for a 4 Ah $LiFePO_4$ battery at low (50 mA) and high (7 A) currents. Full frequency sweeps from 10 µHz to 1 Hz.

Frequency division multiplexing proves superior in stabilizing the impedance spectrum against impedance drift phenomena. That stable impedance agrees most closely with expectations from models [3], [12], [13], [27].

Thus, substantial charge displacement achieved with the frequency domain method appears to stabilize battery impedance more effectively and maximize measured data quality when compared with large peak currents achieved with the time domain method. This implies that it is charge displacement rather than working current value that should be maximized in order to expose the true working impedance of a battery, and to optimize data for ECM fitting. This is consistent with the expectation that surface layer processes on the battery electrodes are responsible for impedance drift; they may also be implicated in the erratic phase behavior seen at ELFs. The exact chemical nature of these interfacial processes requires further clarification.

Acknowledgments

The authors wish to acknowledge the assistance of Waikato-Link and a Waikato University Doctoral Scholarship.

References

[1] A. Lasia, *Electrochemical Impedance Spectroscopy and its Applications*. New York, NY: Springer New York, 2014.

[2] W. Choi, H.-C. Shin, J. M. Kim, J.-Y. Choi, and W.-S. Yoon, "Modeling and Applications of Electrochemical Impedance Spectroscopy (EIS) for Lithium-ion Batteries," *J. Electrochem. Sci. Technol*, vol. 11, no. 1, pp. 1–13, 2020.

[3] T. J. Freeborn, B. Maundy, and A. S. Elwakil, "Fractional-order models of supercapacitors, batteries and fuel cells: a survey," *Mater. Renew. Sustain. Energy*, vol. 4, no. 3, p. 9, Sep. 2015.

[4] D. A. Howey, P. D. Mitcheson, V. Yufit, G. J. Offer, and N. P. Brandon, "Online Measurement of Battery Impedance Using Motor Controller Excitation," *IEEE Trans. Veh. Technol.*, vol. 63, no. 6, pp. 2557–2566, Jul. 2014.

[5] L. Ungurean, G. Cârstoiu, M. V. Micea, and V. Groza, "Battery state of health estimation: a structured review of models, methods and commercial devices," *Int. J. Energy Res.*, vol. 41, no. 2, pp. 151–181, 2017.

[6] M. Cacciato, G. Nobile, G. Scarcella, and G. Scelba, "Real-Time Model-Based Estimation of SOC and SOH for Energy Storage Systems," *IEEE Trans. Power Electron.*, vol. 32, no. 1, pp. 794–803, Jan. 2017.

[7] U. Westerhoff, K. Kurbach, F. Lienesch, and M. Kurrat, "Analysis of Lithium-Ion Battery Models Based on Electrochemical Impedance Spectroscopy," *Energy Technol.*, vol. 4, no. 12, pp. 1620–1630, 2016.

[8] C. Zou, L. Zhang, X. Hu, Z. Wang, T. Wik, and M. Pecht, "A review of fractional-order techniques applied to lithium-ion batteries, lead-acid batteries, and supercapacitors," *J. Power Sources*, vol. 390, pp. 286–296, 2018.

[9] P. Mauracher and E. Karden, "Dynamic modelling of lead/acid batteries using impedance spectroscopy for parameter identification," *J. Power Sources*, vol. 67, no. 1-2, pp. 69–84, 1997.

[10] A. Lasia, "Definition of Impedance and Impedance of Electrical Circuits," in *Electrochemical Impedance Spectroscopy and its Applications*. New York, NY: Springer New York, 2014, pp. 7–66. [Online]. Available: http://link.springer.com/10.1007/978-1-4614-8933-7_2

[11] R. Hasan and J. B. Scott, "Fractional behaviour of rechargeable batteries." Victoria University of Wellington, New Zealand: Electronics New Zealand Inc, Nov. 2016, pp. 111–114. [Online]. Available: https://hdl.handle.net/10289/10756

[12] E. Poihipi, J. Scott, and C. Dunn, "Distinguishability of Battery Equivalent-Circuit Models Containing CPEs: Updating the Work of Berthier, Diard, & Michel," *J. Electroanal. Chem.*, vol. 911, p. 116201, Apr. 2022. [Online]. Available: https://linkinghub.elsevier.com/retrieve/pii/S157266572200193X

[13] J. Scott and R. Hasan, "New Results for Battery Impedance at Very Low Frequencies," *IEEE Access*, vol. 7, pp. 106 925–106 930, 2019.

[14] A. Peinado and A. Fúster-Sabater, "Generation of pseudorandom binary sequences by means of linear feedback shift registers (LFSRs) with dynamic feedback," *Math. Comput. Model.*, vol. 57, no. 11, pp. 2596–2604, 2013.

[15] E. Locorotondo, V. Cultrera, L. Pugi, L. Berzi, M. Pierini, and G. Lutzemberger, "Development of a battery real-time state of health diagnosis based on fast impedance measurements," *J. Energy Storage*, vol. 38, p. 102566, 2021.

[16] A. Guha and A. Patra, "Online Estimation of the Electrochemical Impedance Spectrum and Remaining Useful Life of Lithium-Ion Batteries," *IEEE Trans. Instrum. Meas.*, vol. 67, no. 8, pp. 1836–1849, Aug. 2018.

[17] H. Chaoui, N. Golbon, I. Hmouz, R. Souissi, and S. Tahar, "Lyapunov-Based Adaptive State of Charge and State of Health Estimation for Lithium-Ion Batteries," *IEEE Trans. Ind. Electron.*, vol. 62, no. 3, pp. 1610–1618, Mar. 2015.

[18] D. V. Do, C. Forgez, K. El Kadri Benkara, and G. Friedrich, "Impedance Observer for a Li-Ion Battery Using Kalman Filter," *IEEE Trans. Veh. Technol.*, vol. 58, no. 8, pp. 3930–3937, Oct. 2009.

[19] B. Saha, K. Goebel, S. Poll, and J. Christophersen, "Prognostics Methods for Battery Health Monitoring Using a Bayesian Framework," *IEEE Trans. Instrum. Meas.*, vol. 58, no. 2, pp. 291–296, Feb. 2009.

[20] Y. Cui, P. Zuo, C. Du, Y. Gao, J. Yang, X. Cheng, Y. Ma, and G. Yin, "State of health diagnosis model for lithium ion batteries based on real-time impedance and open circuit voltage parameters identification method," *Energy*, vol. 144, pp. 647–656, 2018.

[21] J. Jiang, Z. Lin, Q. Ju, Z. Ma, C. Zheng, and Z. Wang, "Electrochemical Impedance Spectra for Lithium-ion Battery Ageing Considering the Rate of Discharge Ability," *Energy Procedia*, vol. 105, pp. 844–849, 2017.

[22] J. Kim, L. Krüger, and J. Kowal, "On-line state-of-health estimation of Lithium-ion battery cells using frequency excitation," *J. Energy Storage*, vol. 32, p. 101841, 2020.

[23] Q. Yang, J. Xu, X. Li, D. Xu, and B. Cao, "State-of-health estimation of lithium-ion battery based on fractional impedance model and interval capacity," *Int. J. Electr. Power Energy Syst.*, vol. 119, p. 105883, 2020.

[24] A. Lasia, "Dispersion of Impedances at Solid Electrodes," in *Electrochemical Impedance Spectroscopy and its Applications*. New York, NY: Springer New York, 2014, pp. 177–201.

[25] R. Hasan and J. Scott, "Application of Swingler's method for analysis of multicomponent exponentials with special attention to non-equispaced data," in *2016 IEEE 12th International Colloquium on Signal Processing & Its Applications (CSPA)*. Melaka, Malaysia: IEEE, Mar. 2016, pp. 12–15. [Online]. Available: http://ieeexplore.ieee.org/document/7515794/

[26] J. B. Scott and P. Single, "Compact nonlinear model of an implantable electrode array for spinal cord stimulation (SCS)," *IEEE Trans. Biomed. Circuits Syst.*, vol. 8, no. 3, pp. 382–390, 2013.

[27] R. Hasan and J. Scott, "Extending Randles's Battery Model to Predict Impedance, Charge–Voltage, and Runtime Characteristics," *IEEE Access*, vol. 8, pp. 85 321–85 328, 2020.

[28] P. E. Pascoe and A. H. Anbuky, "The behaviour of the coup de fouet of valve-regulated lead–acid batteries," *J. Power Sources*, vol. 111, no. 2, pp. 304–319, Sep. 2002.

[29] H. Budde-Meiwes, J. Kowal, D. U. Sauer, and E. Karden, "Influence of measurement procedure on quality of impedance spectra on lead–acid batteries," *J. Power Sources*, vol. 196, no. 23, pp. 10 415–10 423, 2011.

[30] V. Farrow, "Characterisation of rechargeable batteries: addressing fractional ultralow-frequency devices," Master of Engineering, University of Waikato, Hamilton, New Zealand, Sep. 2020.

[31] J. Scott and A. Parker, "Distortion analysis using SPICE," *J. Audio Eng. Soc.*, vol. 43, no. 12, pp. 1029–1040, Dec. 1995.

[32] J. A. Nelder and R. Mead, "A Simplex Method for Function Minimization," *Comput. J.*, vol. 7, no. 4, pp. 308–313, Jan. 1965.

[33] W. H. Press, *Numerical recipes in C: the art of scientific computing*, 2nd ed. Cambridge, UK: Cambridge University Press, 1992.

VI. Biography Section

Christopher Dunn is a PhD student at the University of Waikato, New Zealand. His background is originally in the pharmaceutical sciences, with past specialization in medicinal chemistry (notably quantitative structure-activity relationships and pharmaceutical analysis), pharmaceutical technology, small-scale and aseptic/sterile manufacturing and quality assurance. He has also worked in scientific communications and in asset management/inspection and line structure engineering for the power supply industry. He holds bachelor's and master's degrees from Portsmouth School of Pharmacy and the Queen's University of Belfast, UK, and a Graduate Diploma in Electronics from the University of Waikato.

Jonathan Scott is the Foundation Professor of Electronic Engineering at the University of Waikato, New Zealand. His research interest is characterization and modeling of implantable electrodes, semiconductor devices, batteries, and acoustic systems. From 1998 to 2006 he was with the Hewlett-Packard and Agilent Technologies Microwave Technology Center in Santa Rosa, California, where he was responsible for advanced measurement systems operating from dc to millimeter-wave. In 1997 and 1998 he was Chief Engineer at RF Technology in Sydney. He was with the University of Sydney in the Department of Electrical Engineering prior to 1997. Professor Scott holds five degrees, has authored over 150 refereed publications, several book chapters and a textbook, and he holds a dozen patents, several covering active products. Professor Scott's educational interests include Threshold Concepts and their application, particularly across engineering disciplines.